

ADAPTIVE FILTERING OF RFI IN WIDEBAND RADARS USING THE LMS ALGORITHMS. PART I: THE TDLMS ADAPTIVE FILTER

Charles TC Le, Scott Hensley, and Elaine Chapin

Jet Propulsion Laboratory
California Institute of Technology
4800 Oak Grove Drive
Mail Stop: 300-235
Pasadena, CA 91109

Phone: (818) 354-4633. Fax: (818) 393-5285. Email: cle@radar-sci.jpl.nasa.gov

Abstract

We apply the time-domain least-mean-square (TDLMS) adaptive filter to suppress narrow-band radio-frequency interference (RFI) in wideband radars. Simulation is used to show the working principles of the adaptive filter. The filter performance with respect to the filter parameters (filter length, delay, and step-size) is analyzed in terms of the radar performance parameters such as the integrated sidelobe ratio (ISLR) and peak sidelobe ratio (PSLR). Finally, the algorithm is tested with P-band synthetic aperture radar (SAR) data collected by the NASA/JPL airborne SAR (AIRSAR) in different noisy environments.

1 Introduction

The dual requirement of a low radar frequency for foliage and/or ground penetration and a wide radar bandwidth for high resolution in wideband radar systems leads to radars operating in fre-

quency bands occupied by other radio systems, such as radio communications, navigation, police, emergency rescue, Table 1 gives the radio frequency allocation as determined by the FCC [1] (this can be viewed online at <http://www.ntia.doc.gov/osmhome/redbook/redbook.html>) and Table 2 shows the operating bandwidths of some wideband systems. To see the potential damage RFI may cause to SAR image quality, Fig. 1 plots the average range spectrum of a NASA/JPL P-band AIRSAR scene (Mount Sonoma) near Petaluma, California, and Fig. 2 displays the heavily contaminated image. The RFI energy is spread out over the whole scene, displaying artifacts and masking target's presence (roads, streets, small stand-alone objects, ...), specially in the low SNR region (upper right corner). The RFI artifacts in Fig. 2 are especially obvious when contrasted with Fig. 3, the same scene filtered by the TDLMS. Any subsequent data processing such as terrain classification, polarimetry, or interferometry would be degraded by the presence of RFI. Thus, suppressing RFI's energy spikes in the spectrum while minimizing signal distortion is necessary to produce high quality SAR products.

The problem of removal or enhancement of narrow-band interference from wideband signals has long been an active research topic in various disciplines. Examples can be found in the signal processing [2], communications [3], and lately in radar [4, 5, 6, 7] and image processing [8] communities. Adaptive filters [9, 10] have played a vital part in solving this problem. The most popular adaptive filtering technique is the least-mean-square (LMS) algorithm, which has enjoyed enormous popularity due to its good compromise for the convergence speed, final misadjustment, stability, complexity and adaptability that are usually required at the same time. This algorithm utilizes a gradient search technique to determine the filter coefficients which minimize the mean square prediction error [9]. The LMS algorithm requires only $2N$ operations per iteration for real data (N for complex data) and no explicit determination of the correlation coefficients of the input data [11]. To justify the need for using adaptive filtering, Fig. 5 shows the cumulative and block spectra of a scene. The cumulative spectrum displays the energy of *all* the RFI sources averaged over 100,000 radar pulses. In contrast, the block spectrum averages only 50 radar pulses per block. It can be seen from the block spectrum that RFI energy is highly non-stationary in time, thus justifying the employment of adaptive filtering. Similar observations can be obtained from Fig. 5 that shows similar cumulative and block spectra of another scene.

The time-domain least-mean-square adaptive filter in Fig. 6 can be intuitively described as follows. The delay Δ causes decorrelation between the wideband components (radar signal) of the primary input d and the reference input x . The adaptive filter estimates the narrow-band component y corresponding to the RFI signal, effectively forming an equivalent transfer function, which is similar to that of narrow-band filters centered at the frequencies of the narrow-band components of the input signal. The wideband component of the delayed input is rejected, while the phase difference of the narrow-band components is readjusted so that they cancel each other at the summing junction, producing a minimum error signal consisting of mainly the wideband component. Uses of the TDLMS adaptive filter to detect signals (such as sinusoids, narrow-band and chirp-like signals, ...) in white Gaussian noise have been described in [11].

In this study, we will apply the TDLMS algorithm to remove narrow-band RFI from wideband SAR signals. We first describe the point target simulator. Then, the stability and convergence of the filter are analyzed in detail in terms of the filter parameters (filter length, delay, and step-size) and input characteristics (signal bandwidth, sampling rate, and SNR). It has been shown that the filter output converges more rapidly than the filter weights [11]. Consequently, the evaluation of the filter performance is based on the SAR compressor output with the help of the radar parameters, such as ISLR and PSLR. Finally, we show cleaned images obtained by applying the adaptive filter to P-band data collected by the NASA/JPL TOPSAR/AIRSAR system [12, 13] and processed with the interferometric SAR processor developed at JPL [14]. Future efforts are included in the conclusion section. Some of the results have been presented in [15, 16].

2 The TDLMS Algorithm

The TDLMS adaptive filter shown in Fig. 6 consists of an L -weight linear prediction filter in which the coefficients $w_l(k)$ are adaptively updated at the input sampling rate, f_s . We define the L -element input \mathbf{d} and weight vectors \mathbf{w} as

$$\mathbf{d}(n) = [d(n), d(n-1), \dots, d(n-L+1)]^T \quad (1)$$

$$\mathbf{w}(n) = [w_0(n), w_1(n), \dots, w_{L-1}(n)]^T \quad (2)$$

The superscript T denotes the matrix transpose. In the RFI suppression problem, a reference signal is obtained by delaying the received signal $d(n)$ to give $x(n) = d(n - \Delta)$ for some time delay Δ . The output of the filter is a linear combination of these delayed past input values weighted by the filter weight vector

$$y(n) = \mathbf{w}^T(n) \cdot \mathbf{x}(n) = \mathbf{w}^T(n) \cdot \mathbf{d}(n - \Delta) \quad (3)$$

This gives an estimate of the RFI signal. The prediction error, which is the radar signal of interest, is obtained by subtracting the RFI estimate y from the received signal d

$$e(n) = d(n) - y(n) \quad (4)$$

The value of Δ is chosen to remove the correlation between the wideband components of the input signal $d(n)$ and the (predicted) filter output $y(n)$. The filter weights $\mathbf{w}(n)$ are selected so as to minimize the mean square error (MSE) $E[e^2(n)]$, where $E[\cdot]$ is the expectation operator. The Widrow-Hoff LMS algorithm leads to a recursive relation for updating the weight vector [9, 10]

$$\mathbf{w}(n+1) = \mathbf{w}(n) + \mu \mathbf{x}(n) e^*(n) \quad (5)$$

where μ is the adaptation constant or step-size parameter. This parameter controls the trade-off between convergence speed and final misadjustment [9, 10, 11]. Large values of μ lead to faster convergence at the expense of large final misadjustment. The stepsize is preselected based on the desired performance characteristics which, in our case, are the radar performance parameters.

The behavior of the LMS adaptive filter has been extensively studied and well published in the literature (see [9, 10, 11] and the references therein). Here, we only give a summary of the main features and important results. Let λ_n be the eigenvalues associated with the input correlation

matrix $\mathbf{R}_{\mathbf{d}\mathbf{d}} = \langle \mathbf{d}(\mathbf{n})\mathbf{d}^H(\mathbf{n}) \rangle$, where \mathbf{d} was defined in Eq. 1 and the superscript H denotes complex conjugate transpose. Then, the learning time of the adaptive filter for each mode is

$$\tau_n = \frac{1}{4\mu\lambda_n} \quad (6)$$

With one sinusoid in white Gaussian noise, the convergence time can be expressed as

$$\tau = \frac{1}{2\mu\sigma_n^2 \left(1 + \frac{L}{2}SNR\right)} \quad (7)$$

where σ_n is the average noise power and SNR is the signal-to-noise ratio. We note that in our RFI problem σ_n is the power of the radar signal, that is, the radar signal is treated as noise as far as the adaptive filter concerns. The SNR will then be the interference-to-signal-to-noise ratio (ISNR). Another important parameter is the final misadjustment error (after convergence). It is defined to be the ratio of the mean-squared error produced by the LMS algorithm to the minimum mean-squared error produced by the optimum Wiener filter. Its expression can be approximated as

$$\mathcal{M} = \frac{\mu L \lambda_{av}}{2} \quad (8)$$

where λ_{av} is defined as the *average eigenvalue* of the input correlation matrix $\mathbf{R}_{\mathbf{d}\mathbf{d}}$

$$\lambda_{av} = \frac{1}{M} \sum_{i=1}^M \lambda_i \quad (9)$$

3 The Point-Target Simulator

The point-target simulator, used in verifying the algorithm and making parameter selections, is shown in Fig. 7. The radar's parameters are specified in the top-left corner. Inputs consist of the radar bandwidth, chirp slope, pulse length, and the caltone's amplitude and frequency. Future wideband radar systems may need to notch certain radio frequencies as required by the FAA, FCC,

and military [17, 18]. This requirement is also implemented in the simulator by specifying the types (FIR or IIR) of the notch filter together with its frequency locations and stopbands. Noise consists of thermal random noise, discrete sinusoidal tones, terrestrial narrow-band modulation signals (AM, FM, ...), and satellite communication signals (ASK, PSK, QASK, FSK, MSK, ...). They are characterized by their amplitudes, frequency locations, and bandwidths with respect to the radar signal. Their initial phases are picked from a uniform distribution of random phase. (In the future GeoSAR system (operational in Sept. 1999), a sniffer pulse is used to measure the RFI environment, so that this feature is also included in the simulator.) The combined radar-and-noise signal is fed into an A/D converter using either 8-bit or block-floating-point quantization (BFPQ) scheme. The A/D output is the input to the LMS adaptive filter which gives as its outputs the estimated RFI signal and the cleaned radar signal. Fig. 8 shows the time-domain waveforms and frequency spectra of the components of a simulated signal. The chirp signal has a bandwidth of 40 MHz and its signal-to-noise ratio (SNR) is 10 dB. The RFI consists of six tones and two FM signals. The tones are at frequencies ± 3 , ± 10 , and ± 15 MHz, with amplitudes (interference-to-signal ratio, ISR) 12, 13, and 17 dB, respectively. The FM signals have center frequencies of ± 12 MHz, with bandwidths of 100 kHz (typical for FM radio channels), and ISRs of 15 dB. The initial phases of all RFI signals are picked at random.

4 Simulation Results, Performance Analysis, and Real Images

4.1 Simulation Results and the Radar Parameters

Fig. 9 compares the signal waveforms and spectra of the input, output, and ideal signals (in the absence of RFI, containing just the radar signal and random Gaussian noise). As evident from the output spectra, most of RFI energy has been removed and the output waveform is close to the ideal case. Fig. 10 shows the outputs of the pulse compression filter for the unfiltered, filtered, and ideal radar signals. The presence of RFI makes it difficult to detect the target (top graph). The adaptive filter helps in reducing the sidelobe energy and enhance the target visibility (middle graph). The compressor output of the filtered signal compares favorably with the ideal case (bottom graph). In order to evaluate the algorithm, it is necessary to define some performance parameters. Among the parameters useful for characterizing filter performance are the ISLR and PSLR. The ISLR is the

ratio of the energy in the sidelobe (SL) to the energy in the main lobe (ML). And the PSLR is the ratio of the peak value of the sidelobe to the peak value of the main lobe. With $g(r)$ denoting the output of the compressor filter, the ISLR and PSLR are defined as

$$ISLR = \frac{\int_{SL} |g(r)|^2}{\int_{ML} |g(r)|^2} \quad (10)$$

$$PSLR = \frac{\max_{SL} \{g(r)\}}{\max_{ML} \{g(r)\}} \quad (11)$$

4.2 Performance with Respect to the Filter Parameters

The design parameters for the LMS adaptive filter are the step-size μ , filter length L , and decorrelation delay Δ . The objective is to study the variation of the performance parameters, ISLR and PSLR, in terms of these design parameters. Since it is difficult to get closed form solution relating these two sets of parameters, one simulation technique is to fix all but one parameter at each simulation stage. For example, we first let $L = 128$, $\Delta = 1$, and study the behavior of ISLR and PSLR as functions of the step-size parameter μ . The results are shown in the top two graphs of Fig. 11. In each graph, the top (circles) and bottom (squares) horizontal dotted lines indicate the limiting values in the cases of an unfiltered and ideal signal; the filter performance (triangles, solid lines) would be somewhere in between, unless the filter is unstable. Both ISLR and PSLR initially take high values for small μ . They then decrease as μ gets larger and reach a minimum at some optimal value of μ . Finally, they increase again at larger values of μ . This can be explained if we recall that the step-size parameter controls the trade-off between convergence speed (inversely proportional to μ , shown in Eq. 6) and final misadjustment (proportional to μ , see Eq. 8). Small values of μ imply slow convergence, leading to large residual RFI energy. On the other hand, large values of μ increase the final misadjustment error and may cause the filter to be unstable. Both cases lead to high ISLR and PSLR. Optimal value of μ for given L and Δ was found to be $\mu = 0.35$. The middle graphs display the ISLR and PSLR as functions of the filter length L for $\mu = 0.35$ and $\Delta = 1$. For short filter lengths, the adaptive filter does not have enough resolution or cannot form sharp notches at the RFIs' frequencies, leading to high signal distortion. Attempting to over-resolve the narrowband signals by increasing the filter length degrades the performance because the final

misadjustment noise is also proportional to the filter length as expressed in Eq. 8. Finally, the bottom graphs plot the ISLR and PSLR in terms of the decorrelation delay Δ for $\mu = 0.35$ and $L = 512$. We note that a delay of one sample is enough to decorrelate the wideband components (radar signals) of the primary and reference inputs. Further increasing of Δ has little effect on the performance. In cases where the signal is oversampled or the radar bandwidth is reduced, it is then necessary to use $\Delta > 1$ to decorrelate the signals. The optimal values for the filter's parameters are $L = 512$, $\mu = 0.1$, and $\Delta = 1$, corresponding to gains of 25 dB and 22 dB for the ISLR and PSLR, respectively (see the bottom graphs in Fig. 11). These optimal values were used to produce the results in Figs. 9 and 10.

4.3 NASA/JPL P-Band TOPSAR/AIRSAR Images

Using the optimal design parameters given above, we have applied the TDLMS adaptive filter to a test site near Petaluma, California. The P-band data (40 MHz bandwidth) has been acquired by the NASA/JPL TOPSAR/AIRSAR instrument [12, 13] in 1996 and processed with an interferometric SAR processor developed at JPL [14]. The average spectra of 100,000 pulses are plotted in Fig. 12. The top spectrum clearly shows the presence of RFI, and the bottom shows the efficacy of our cleaning technique. There remains some RFI energy in the lower and upper limits of the frequency spectrum. Since we are using a Hamming window to compress the signal, the residual RFI energy is greatly attenuated. We also note that the filter preserves the caltone frequency at the far left position of the frequency spectrum (the caltone is essential for good calibration of channels' gains). The range-Doppler image of an agriculture area is shown in Fig. 3. Compared with the RFI-contaminated image in Fig. 2 the cleaned image shows remarkable improvement. First, the target's visibility is greatly enhanced as shown in the left close-up images (denoted as "flat_rfi.gif" and "flat_td.gif") in Fig. 13. This region corresponds to point A in the original image, Fig. 2. We can clearly see the streets and other small stand-alone features which are very hard to detect in the original image. Second, the adaptive filter also removes artifacts due to RFI as demonstrated in the right close-up images (denoted as "hill_rfi.gif" and "hill_td.gif") in Fig. 13. This is region B, an area of rolling hills and pastureland, in the original image, Fig. 2. We observe that it is difficult to distinguish between the real features running NW-SE in the upper left corner and the artificial stripes resulting from spreading of RFI energy. The filtered image is effectively free of

these artifacts, clearly showing rural roads and other features.

5 Conclusion

We have presented an adaptive filtering technique to remove RFI from wideband SAR signals. The filter employs the least-mean-square algorithm to update the filter weights. This weight update scheme requires no matrix solving or calculation of the correlation coefficients. The filter design is very simple since there are only three design parameters. Yet, the filter can adapt to the noisy RFI environment. We have also described the simulation procedure to show the filter's working principle and to obtain the optimal values for the design parameters. Finally, we have displayed the RFI-contaminated image and compared it with a much improved image. Our future efforts include fast versions of the adaptive filter, automatic determination of the design parameters, and assessment of RFI effects in other SAR signal processing involved in image formation, target classification, polarimetry, and interferometry. In particular, part II and III of the paper will discuss the frequency-domain LMS(FDLMS) [19] and filter-bank LMS (FBLMS) [20] approaches.

Acknowledgment: The authors would like to thank Dr. M. Davis of DARPA and Dr. P. Tomlinson of DSA for their continuous support, encouragement, and useful suggestions, Dr. P. Maloney of DSA for his providing of needed background information on the RFI problem, Dr. C. Werner of JPL for his thoughtful discussions, and Mr. A. Chu of JPL for his testing and highly constructive critiques of the proposed techniques. This work has been done at the Jet Propulsion Laboratory, California Institute of Technology, under contract with the National Aeronautics and Space Administration.

References

- [1] "Manual of regulations and procedures for federal radio frequency management", National Telecommunications and Information Administration, US Department of Commerce, 1995.
- [2] B. Widrow, J. Glover, J. McCool, J. Kaunitz, C. Williams, K. Hearn, J. Zeidler, E. Dong, Jr., and R. Goodin, "Adaptive noise cancelling: principles and applications", *Proc. of the IEEE*,

- vol. 63, pp. 1692-1716, 1975.
- [3] L. Milstein, "Interference rejection techniques in spread spectrum communications", *Proc. of the IEEE*, vol. 76, pp. 657-71, 1988.
 - [4] "Chapter 3: Interference Suppression", in *Aspects of Radar Signal Processing*, B.L. Lewis, F.F. Kretschmer, Jr. and W.W. Shelton, Editors, Artech House, 1986.
 - [5] M. Braunstein, J. Ralston, and D.Sparrow, "Signal processing approaches to radio frequency interference suppression", in *Algorithms for Synthetic Aperture Radar Imagery*, Dominick A. Giglio, Editor, *Proc. SPIE*, vol. 2230, pp.190-208, 1994.
 - [6] "Session 3: Radio Frequency Interference Rejection", in *Algorithms for Synthetic Aperture Radar Imagery II*, Dominick A. Giglio, Editor, *Proc. SPIE*, vol. 2487, pp. 72-129, 1995.
 - [7] T. Miller, L. Potter, and J. McCorkle, "RFI suppression for ultrawideband radar", *IEEE Trans. Aerospace Electronic Systems*, vol. AES-33, pp. 1142-56, 1997.
 - [8] T. Soni, J.R. Zeidler, and W.H. Ku, "Performance evaluation of 2-D adaptive prediction filters for detection of small objects in image data", *IEEE Trans. Image Processing*, vol. 2, pp. 327-340, 1993.
 - [9] B. Widrow and S.D. Stearns, *Adaptive Signal Processing*, Englewood Cliffs, N.J.: Prentice-Hall, 1984.
 - [10] S. Haykin, *Adaptive Filter Theory*, Englewood Cliffs, N.J.: Prentice-Hall, 1991.
 - [11] J.R. Zeidler, "Performance analysis of LMS adaptive prediction filters", *Proc. of the IEEE*, vol. 78, pp. 1781-1806, 1990.
 - [12] H. A. Zebker, S. N. Madsen, J. Martin, K. B. Wheeler, T. Miller, Y. Lou, G. Alberti, S. Vetrella, and A. Cucci, "The TOPSAR interferometric radar topographic mapping instrument", *IEEE Trans. Geosci. Remote Sensing*, vol. 30, no. 5, pp. 933-940, 1992.
 - [13] Y. Kim, Y. Lou, J. van Zil, L. Maldonado, T. Miller, T. Sato, and W. Skotnicki, "NASA/JPL airborne three-frequency polarimetric/interferometric SAR system", in *Proc. IGARSS'96*, vol. 3, pp. 1612-14, Lincoln, NE, May 1996.

- [14] P.A. Rosen, "IFSARE processor documentation", Jet Propulsion Laboratory, 1995.
- [15] C.T.C. Le, S. Hensley, and E. Chapin, "Adaptive filtering of RFI in wideband SAR signals", Seventh Annual JPL Airborne Earth Science Workshop, Jet Propulsion Laboratory, Pasadena, CA, January 1998.
- [16] C.T.C. Le and S. Hensley, "RFI rejection in wideband SAR signals using the LMS adaptive filters", *ASAP '98*, the Sixth Annual Workshop on Adaptive Sensor Array Processing, Lincoln Laboratory, Lexington, MA, March 1998.
- [17] T. Koutsoudis and L. Lovas, "Transversal filter approach to RFI removal for the P-3 ultra-wideband SAR", Final Report to DARPA, Northrop Grumman Advanced Technology Development Center, December 1996.
- [18] D.W. Quasny, "Concealed target detection radar EMI analysis", Engineering memorandum to Department of Defense Electromagnetic Compatibility Analysis Center, August 1994.
- [19] C.T.C. Le, S. Hensley, and E. Chapin, "Adaptive filtering of RFI in wideband radars using the LMS algorithms. Part II: the FDLMS adaptive filter.", *IEEE Trans. Aerospace Electronic Systems*, submitted for publication, March 2000.
- [20] C.T.C. Le and S. Hensley, "Adaptive filtering of RFI in wideband radars using the LMS algorithms. Part III: the FBLMS adaptive filter.", *IEEE Trans. Aerospace Electronic Systems*, submitted for publication, March 2000.

Frequency Bands	Usages
9 -- 535 (kHz)	Fixed and mobile (aeronautical, land, maritime) stations
535 -- 1605 (kHz)	AM broadcasting stations
1605 -- 4000 (kHz)	Fixed and mobile stations
4 -- 29.7 (MHz)	Fixed and mobile stations, broadcasting stations, space and earth stations
29.7 -- 108 (MHz)	Fixed and mobile stations, aeronautical radionavigation stations (marker beacons on 75 MHz), FM and TV broadcasting stations, space and earth stations
108 -- 960 (MHz)	Fixed and mobile stations, radiodetermination stations, TV broadcasting stations, space and earth stations
960 -- 1215 (MHz)	Aeronautical radionavigation stations, IFF/ATCRBS of similar type stations
1215 -- 10500 (MHz)	Fixed and mobile stations, radiodetermination stations, space and earth stations

Table 1: Radio frequency allocation.

SAR Systems	Operating Frequencies	Status
NASA/JPL P-Band AIRSAR	407 -- 447 MHz	operational
NASA/JPL L-Band AIRSAR	1217 -- 1257 MHz	operational
P-Band GeoSAR	270 -- 430 MHz	operational in 1999
L-Band SIR-C/X-SAR	10, 20, and 40 MHz	operational
Loral Airborne SAR	500 -- 800 MHz	operational
ERIM UWB P-3 SAR	200 -- 900 MHz	operational
ARL UWB Rail SAR	60 MHz -- 1 GHz	operational

Table 2: Wide- and ultra-wideband SAR systems.

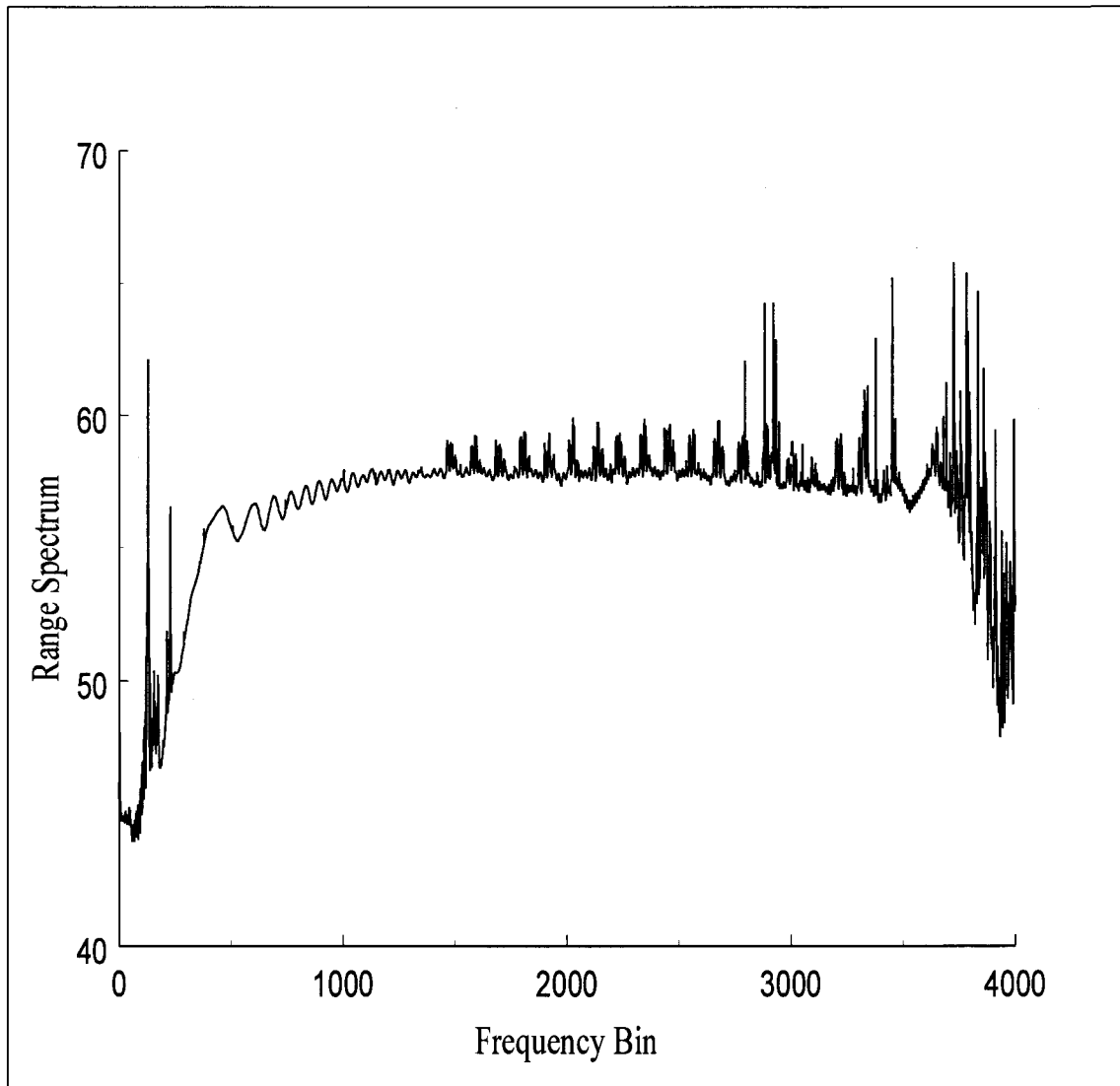


Figure 1: Average range spectrum of 100,000 pulses of a scene (Mount Sonoma) near Petaluma, California.



Figure 2: RFI-contaminated range-Doppler image of Mount Sonoma, California.

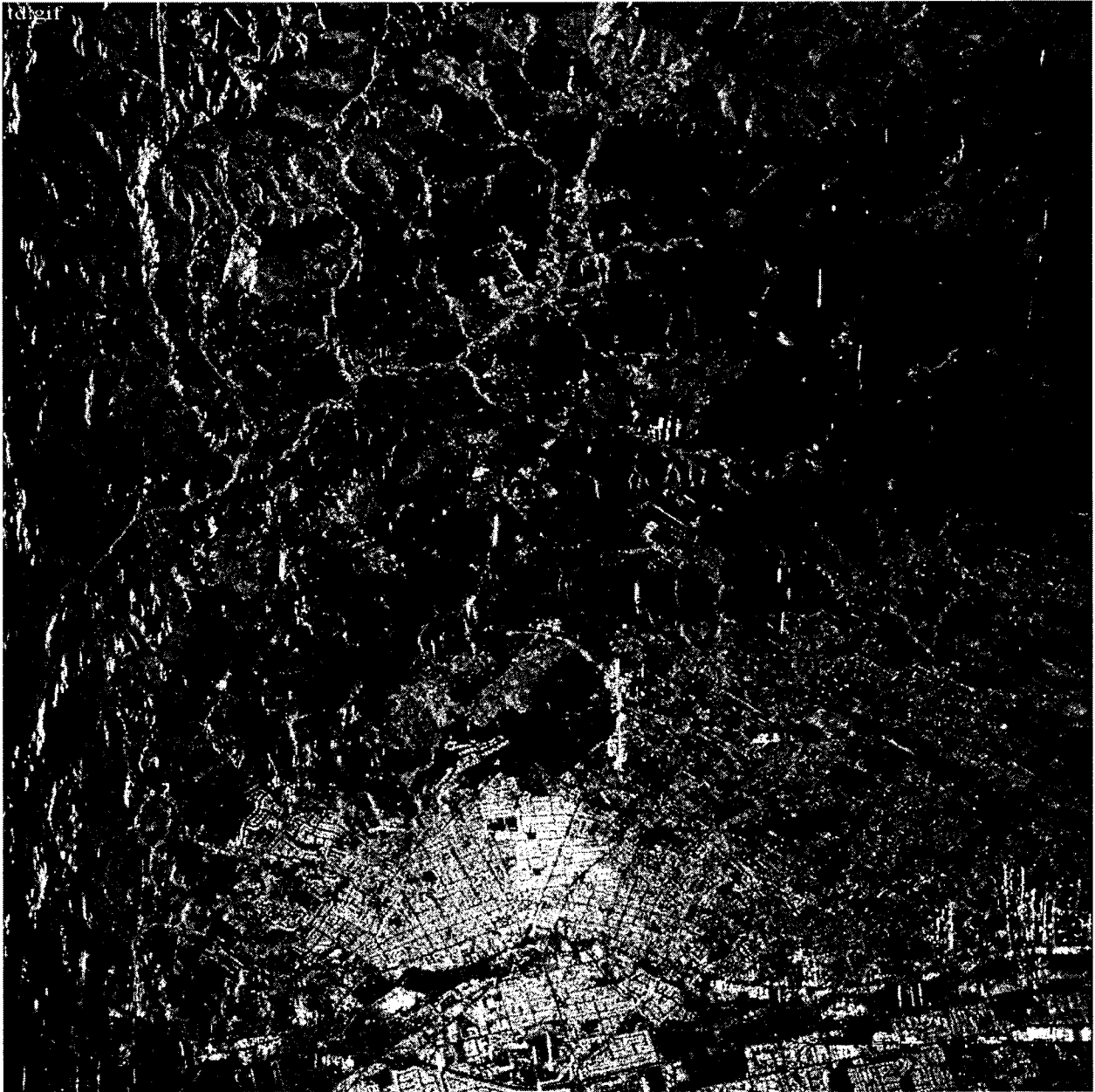


Figure 3: Range-Doppler image of Mount Sonoma, California; cleaned with the TDLMS adaptive filter.

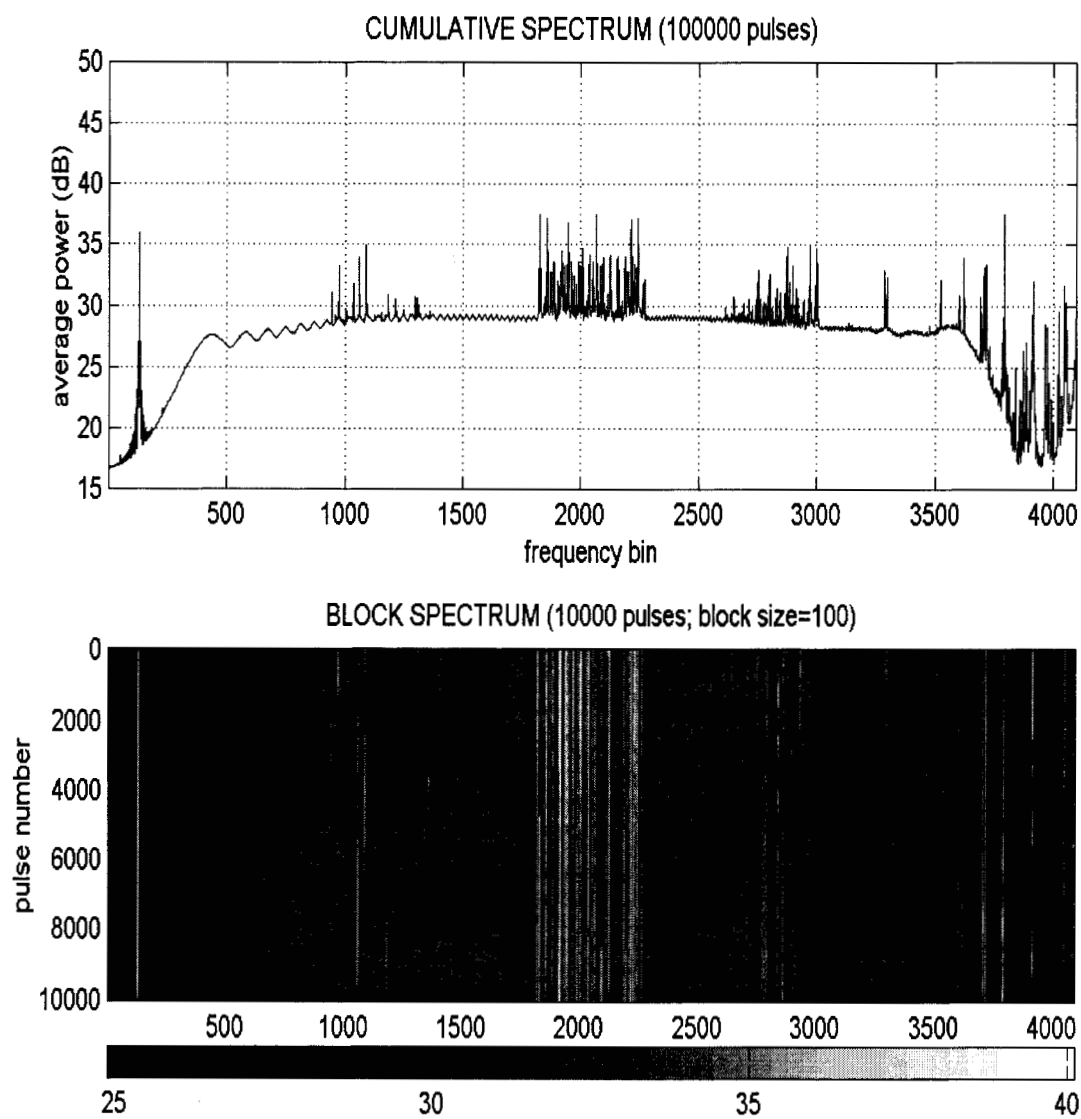


Figure 4: Cumulative (above) and block (below) spectra of a scene.

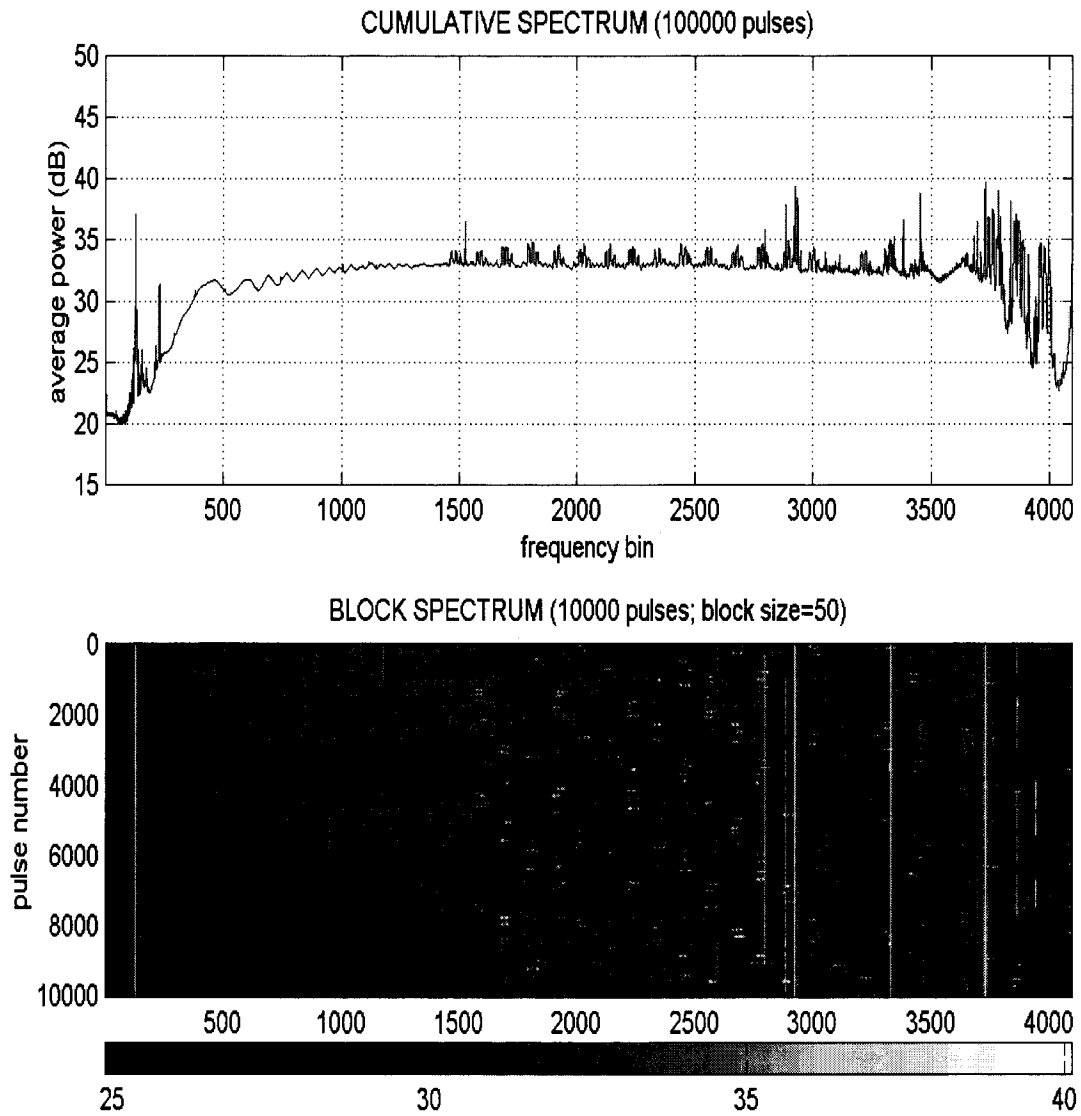


Figure 5: Cumulative (above) and block (below) spectra of a scene.

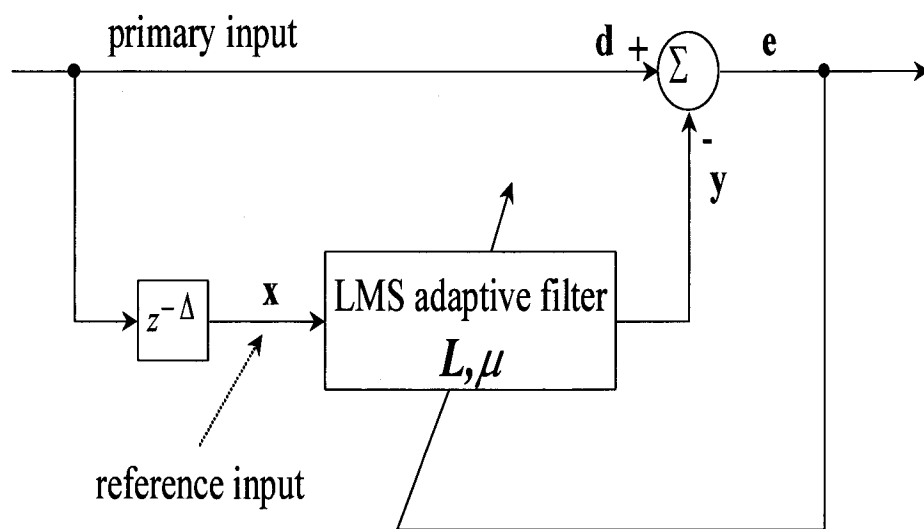


Figure 6: The TDLMS adaptive filter.

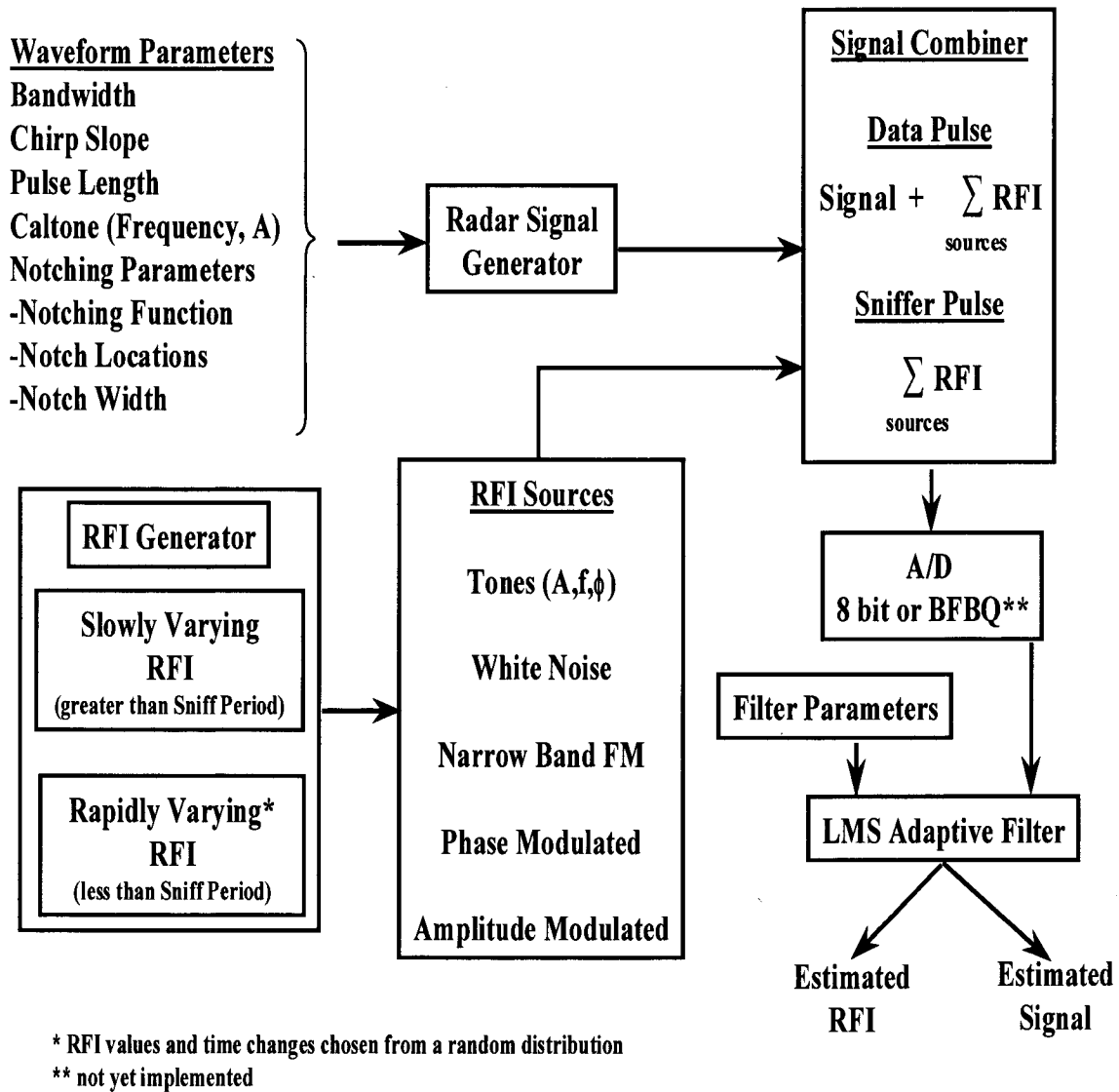


Figure 7: RFI simulator block diagram.

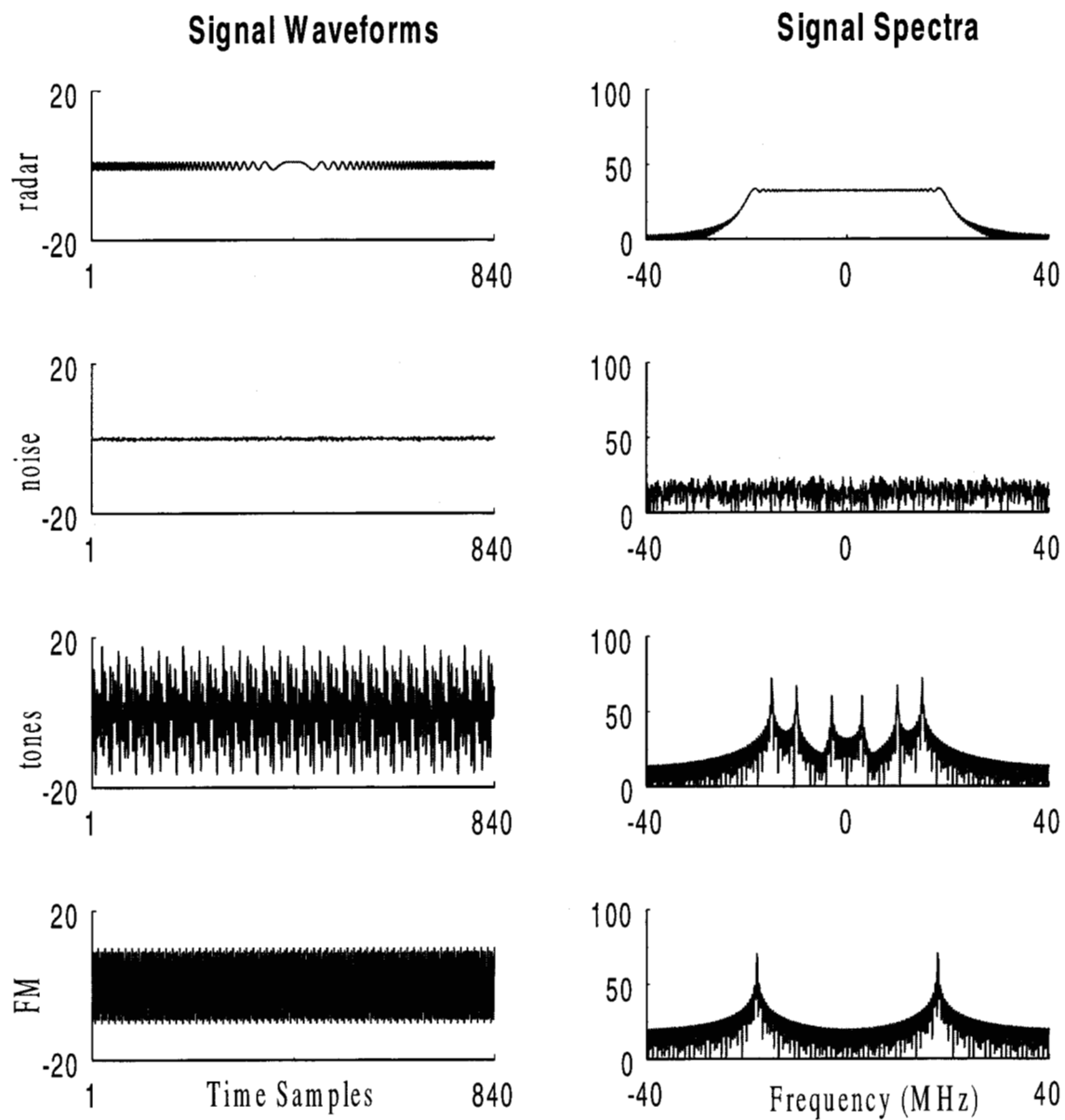


Figure 8: Time-domain and frequency-domain components of input signal.

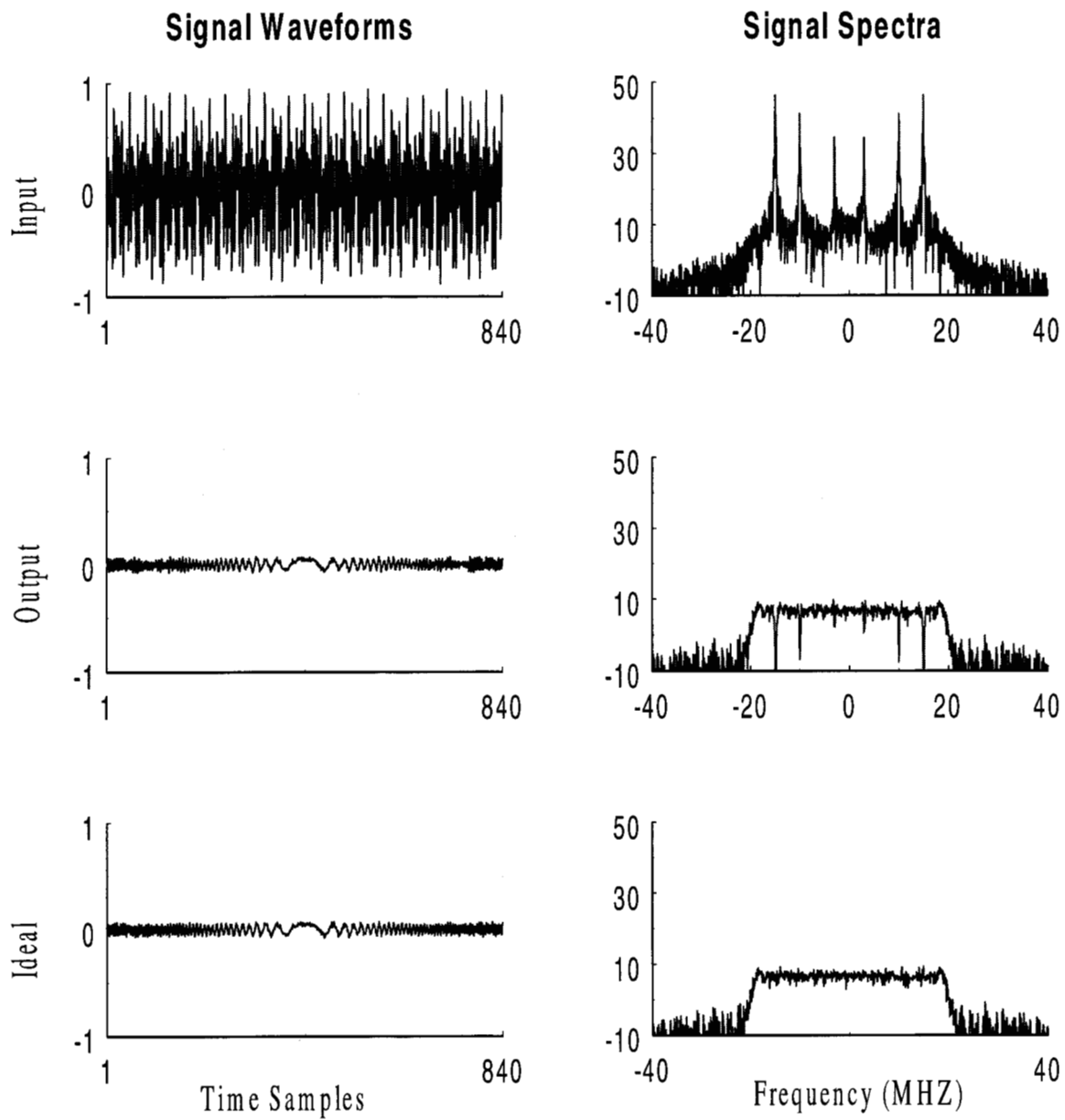


Figure 9: Comparison of signal waveforms and spectra.

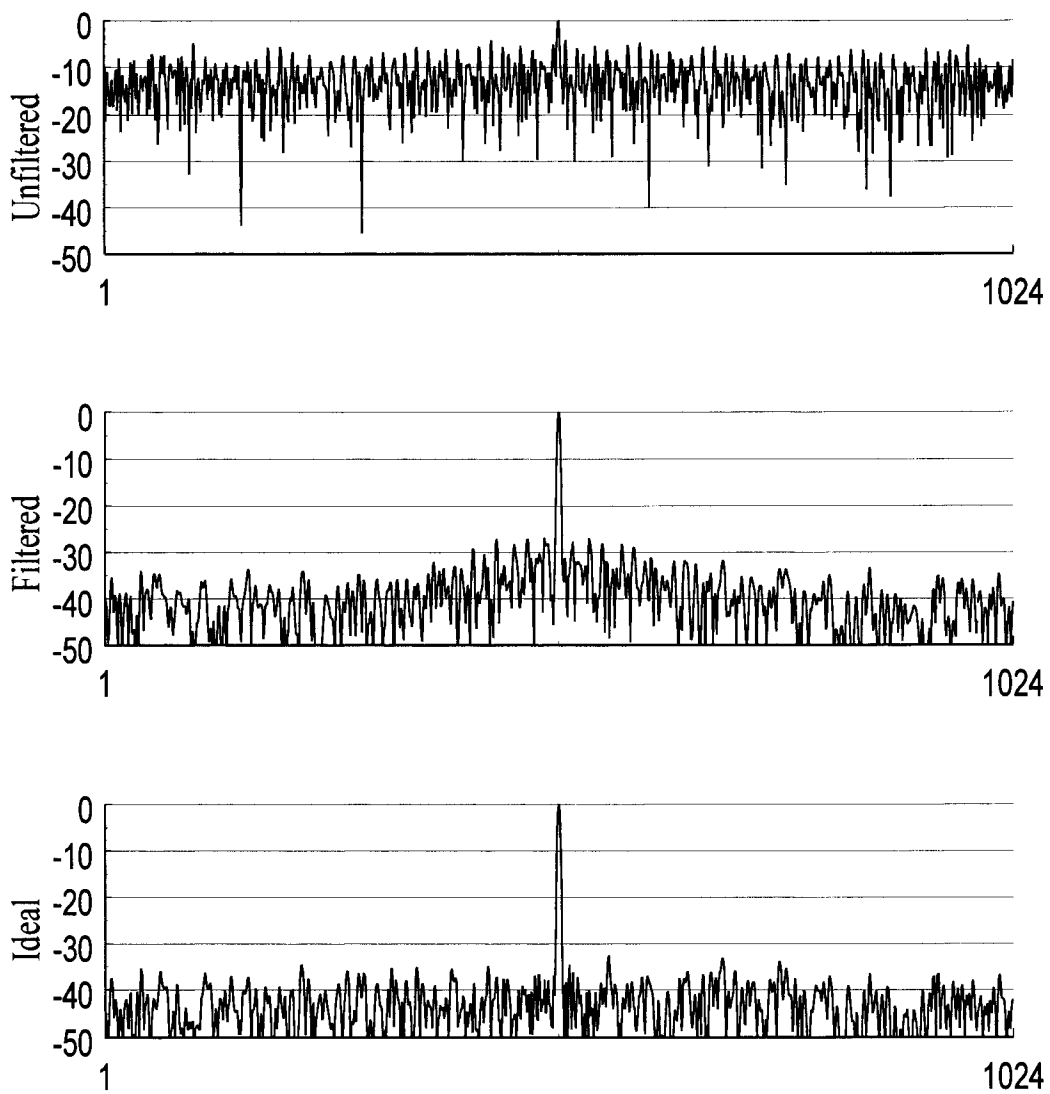


Figure 10: Comparison of outputs of pulse compression filter.

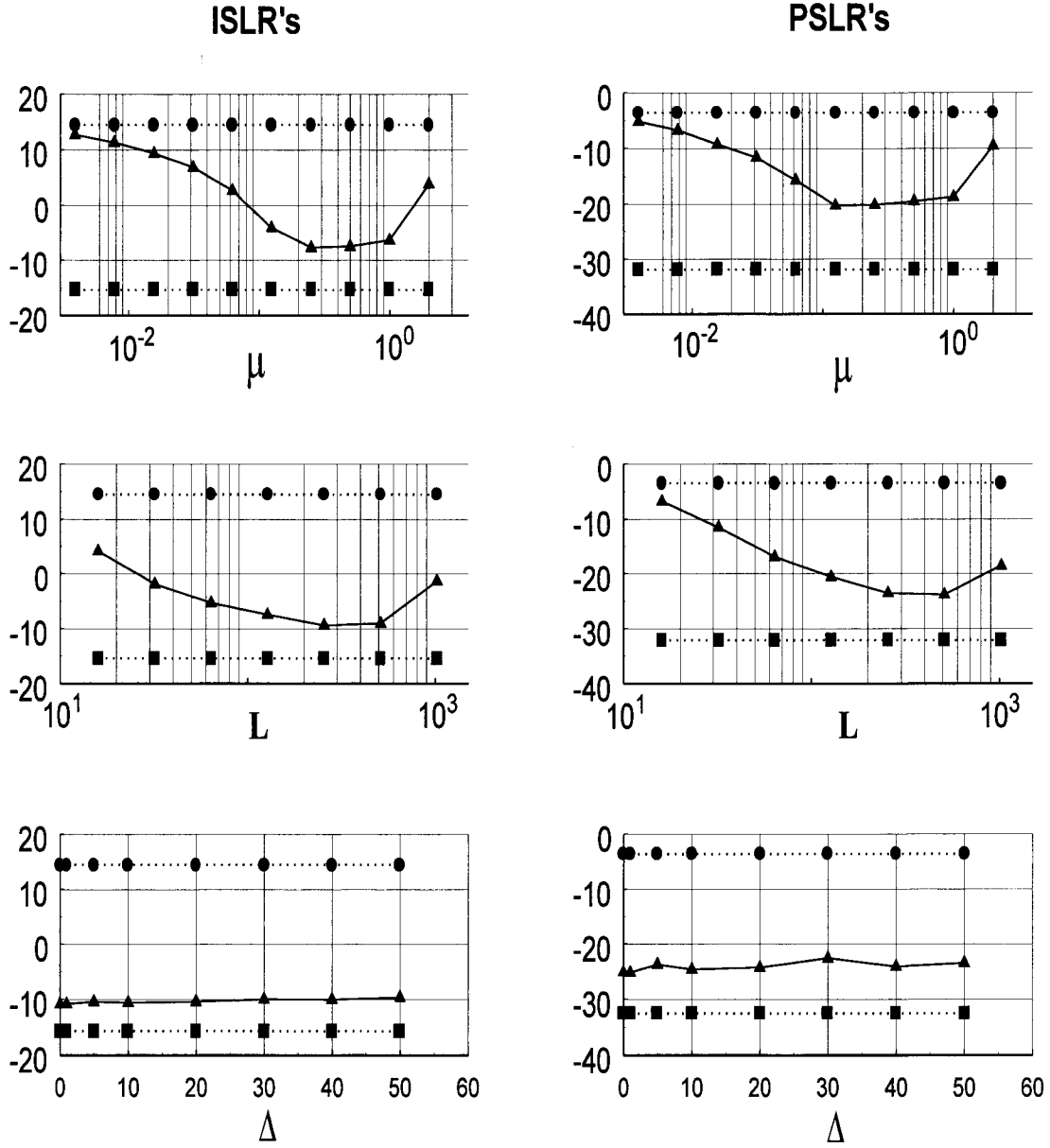


Figure 11: Performance parameters ISLR (left) and PSLR (right) in terms of the step-size parameter μ (top), filter length L (middle), and decorrelation delay Δ (bottom).

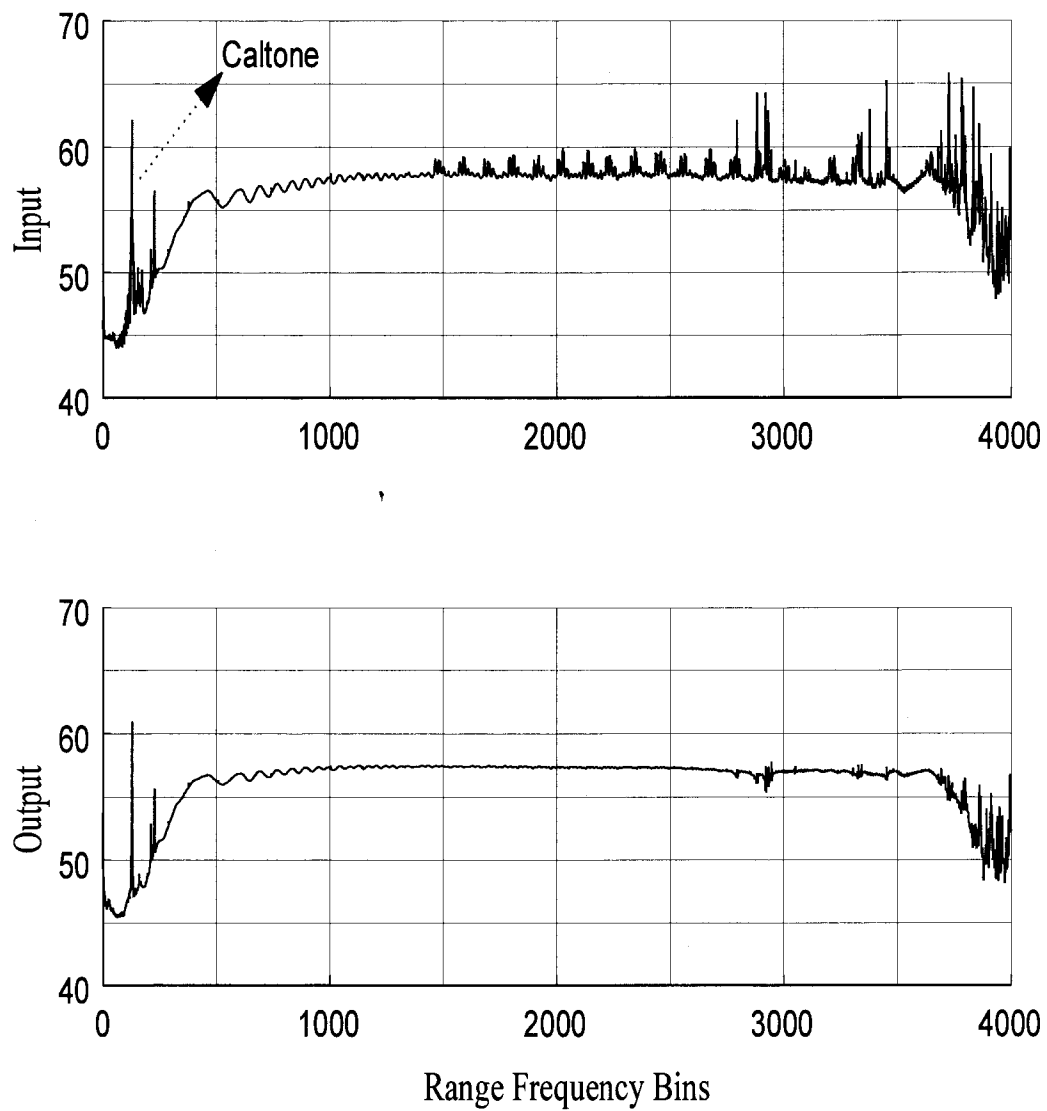


Figure 12: Average spectrum of 100,000 pulses (top: unfiltered, bottom: filtered).

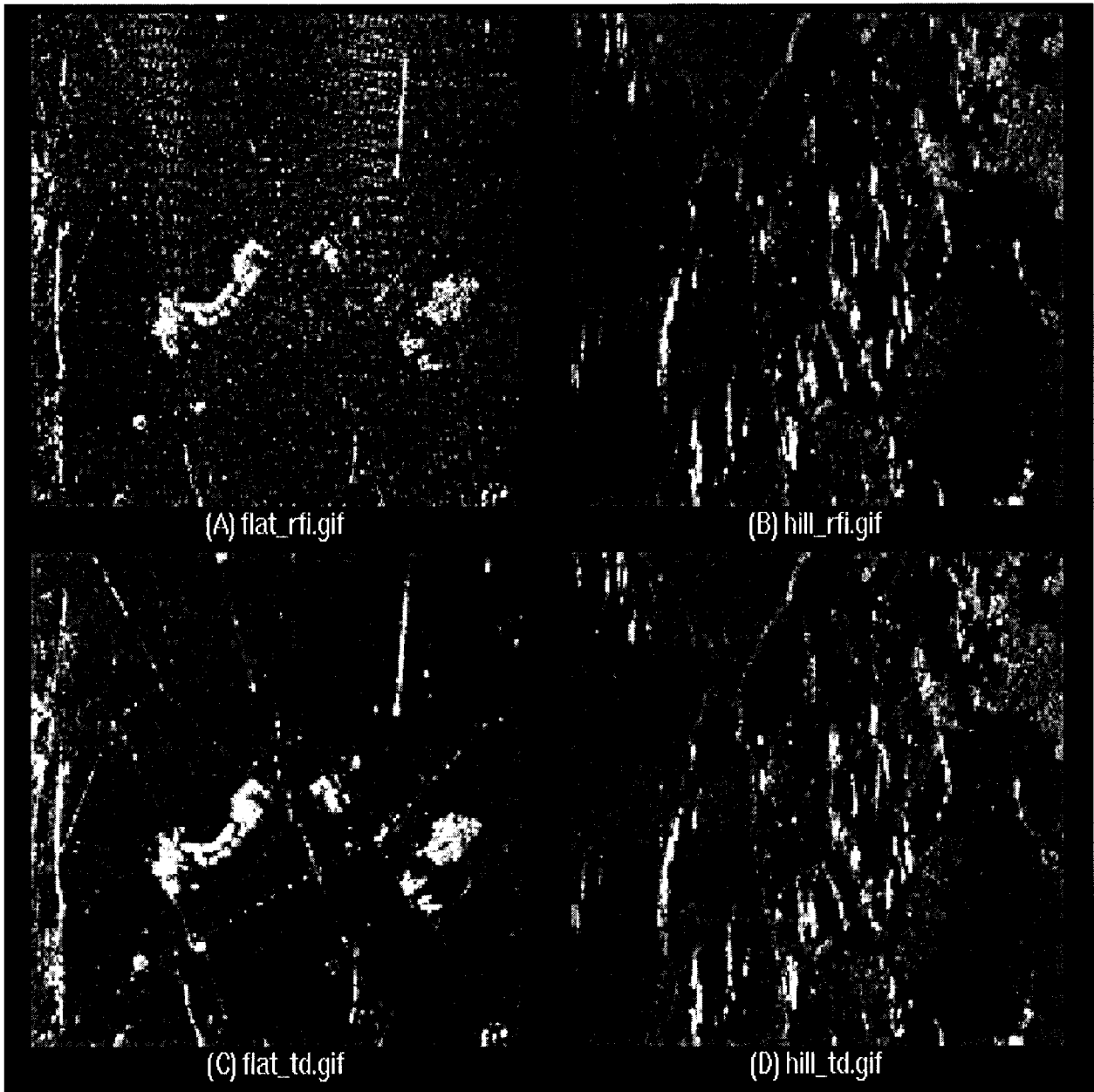


Figure 13: Close-up images of region A and B in Fig. 2.